coatings

MDPI

Article

Effect of Trajectory Curvature on the Microstructure and Properties of Surfacing Wall Formed with the Process of Wire Arc Additive Manufacturing

Tao Feng [1], Lishi Wang [1,*], Zhongmin Tang [2], Shanwen Yu [1], Zhixiang Bu [1], Xinbin Hu [1] and Yihang Cheng [1]

[1] Hubei Provincial Key Laboratory of Green Materials of Light Industry, College of Materials and Chemical Engineering, Hubei University of Technology, Wuhan 430068, China; fengtao9873@163.com (T.F.); swyu13387511463@163.com (S.Y.); bzxwh@hbut.edu.cn (Z.B.); huxbshu@163.com (X.H.); hbutchengyihang@163.com (Y.C.)

[2] Hubei Sanjiang Aerospace Hongyang Electromechanical CO. LTD, Xiaogan 432100, China; yaweitang@163.com

* Correspondence: lswang@hbut.edu.cn; Tel.: +86-27-59750482

Received: 4 November 2019; Accepted: 6 December 2019; Published: 11 December 2019

Abstract: Curvature effects are typically present in the process of additive manufacturing (AM), particularly for wire arc additive manufacturing. In this paper, stainless-steel wire was adopted to deposit thin-walled samples with different curvatures. Optical microscopy, SEM, EDS and micro-hardness was used to analyse the microstructure, composition and properties of the samples. The result shows that the bottom region of the thin-walled sample had a mainly planar and cellular crystal microstructure. For the middle region, the microstructure revealed mainly dendrites, and the top layer has equiaxed dendrite morphology. The microhardness value of the bottom was greater than that of the middle, and the microhardness value of the middle was greater than that of the top. Moreover, the grain size of the inner part (direct to curvature radius) was larger than that of the outer part, and the micro-hardness value exhibited an increasing tendency from the inner to the outer side. With enlarging curvature, the degree of grain size differences and micro-hardness variants decreased. Finally, an investigation with a low carbon steel wire showed that it had a similar curvature effect for its AM specimen.

Keywords: wire arc additive manufacturing; curvature effect; microstructure and properties

1. Introduction

Additive manufacturing (AM), also known as rapid forming technology, was proposed by Charles W. Hul in the 1980s [1]. "AM as a process of joining materials to make objects from 3D model data, usually layer upon layer, as opposed to subtractive manufacturing methodologies" [2]. Compared with traditional machining operations and other manufacturing technologies, additive manufacturing technology can quickly and accurately manufacture complex parts with high forming efficiency, which can save design and manufacturing costs, to a certain extent [3–5]. The heat sources used in additive metal manufacturing include lasers, electron beams, arcs, etc. [6–12]. Frequently used AM materials are Polymers, ceramics and metals [13,14]. Recently, AM has been widely used in various industries, such as aerospace. The AM process has been used to produce the central flange of the Chinese-made aircraft C919. The selective laser melting process is also used in the renovation and coating of precision parts [15]. The AM process plays an important role in Industry 4.0, because it saves time and has lower costs [16]. Compared to laser and electron beam AM, wire arc additive manufacturing (WAAM) equipment, with its low cost and high forming efficiency, is suitable for manufacturing large components [17–19].

In the process of arc additive manufacturing, it is complicated by the thermal effect of the arc pre-deposited adjacent region being reheated with subsequent welding passes [20,21]. Besides, the heat accumulation during the forming process has different effects on the microstructure and properties of formed parts. Therefore, in industrialized applications of WAAM technology, it is valuable to understand the influence of the arc thermal effect on the microstructure and performance of different zones of the formed parts. Liu et al. [22] prepared single-layer multilayer samples at different deposition rates. The results show that the mechanical properties could be much improved with a suitable deposition rate, because it has a finer and more uniform microstructure. Zhou et al. [23], studied the effect of an external magnetic field on the microstructure and mechanical properties of shaped specimens. They found that the microstructure was more uniform, and the mechanical properties were superior than when utilizing an external magnetic field. Ge et al. [24] studied the thermal history, microstructure and properties of formed parts in different locations, showing that the preheating effect from previously built layers can be effectively used to reduce residual stresses. The cooling rate firstly decreased rapidly, and then kept stable near the top layer. The parts can be a straight wall or a block, and they can also be curved. Thus, it is usually inevitable to have a curved traveling path for additive manufacturing. The presence of a curve may result in a difference in performance between the inside and outside of the curve. For example, under aerospace or high temperature and high-pressure conditions, it may be necessary to carry out some intensive treatment measures on the side with poor performance. Specific and in-depth analysis of the influence of the curvature of the path on the microstructure and properties of fabricated parts, is still lacking. Stainless-steel components with a complex structure are widely used in the industry. Meanwhile, WAAM provides a novel processing method option for them. This paper investigates the effect of trajectory curvature on the microstructure and mechanical properties of thin-walled samples with a 304 stainless-steel wire arc additive manufacturing process. Moreover, low carbon steel wire was used to verify the effect of curvature on WAAM structure and performance.

2. Experimental

The stainless-steel wire used in the experiment was ER304. The wire diameter was 1.0 mm, and the substrate material was Q235 steel plate. The composition of the welding wire and substrate material is shown in Table 1. The oxide film on the surface of the substrate plate was cleaned with mechanical methods, and then wiped with acetone before welding. The additive manufacturing system used here consisted mainly of the Megmid MIG500 welder (Shenzhen, China) and the ABB1410 robot (Zurich, Switzerland), as shown in Figure 1. The sample was reciprocally deposited without pre-heating before welding, and each pass had a fixed curvature.

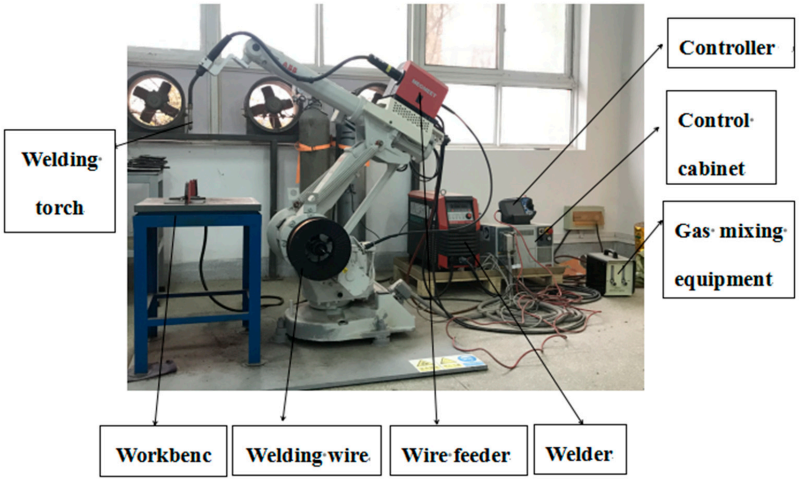

Figure 1. The system in site used for wire arc additive manufacturing.

The path curvature of the experimental parts is shown in Figure 2. The sample was cut with a wire-cut electrical discharge machine (DK7750, Star peak, Taizhou, China). The metallographic etching solution for stainless-steel consisted of nitric acid, hydrofluoric acid and glycerine, and their volume ratio was 1:2:1. The sample was etched by swabbing with the solution until the boundary between the layers was clearly displayed. Next, the transverse hardness measurement was performed on the first, fifth and tenth layers, from the left (inside) side to the right (outside), using a Vickers hardness tester (THVS-1MDX-AXY, Qifeng, Chengdu, China). The conditions of the hardness test had a point interval of 0.03 mm, a load of 200 g, and a dwell time of 10 s. Finally, the sample was polished and etched again by swabbing, in order to observe the metallographic structured with a metallographic microscope (Olympus GX51, Tokyo, Japan).

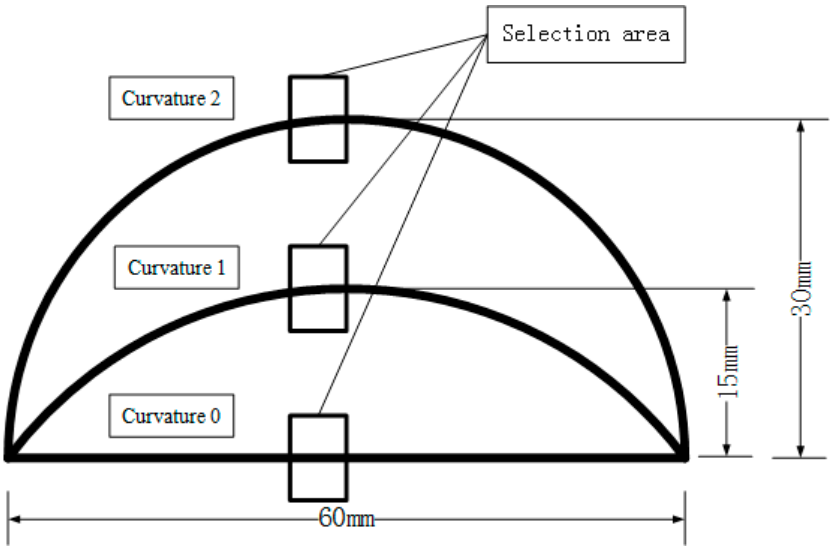

Figure 2. Traveling paths for three-types of curvature samples.

The traveling path of low carbon steel (ER50-6, the composition of the welding wire is shown in Table 1) was the same as the stainless-steel welding wire, in terms of deposited layers. The metallographic etching solution for low carbon steel contained 4% (*v*/*v*) nitric acid alcohol.

Table 1. Composition of welding wire and substrate material.

Chemical Composition (wt %)	Wire Type		Substrate Material
	ER304	ER50-6	Q235
C	0.10	0.06–0.15	0.12–0.20
Si	0.65	0.80–1.15	≤0.30
Mn	1.72	1.40–1.85	0.30–0.65
Cr	17.5	≤0.15	–
Ni	9.3	≤0.15	–
P	–	≤0.025	≤0.045
S	–	≤0.025	≤0.045

At the first stage, the investigation was carried out with a large number of basic technological experiments, such as using single-pass single-layer and single-pass multi-layer. We compared and analysed the morphology (weld height, weld width, etc.) of the single-pass single-layer, and the depositing effect and the dimensional accuracy of the single-pass multi-layer forming test, under different technological parameters. Some single-layer single-pass weld shapes with various process parameters are shown in Figure 3. The process parameters were gradually adjusted to get a stable geometric weld for ER304 stainless-steel welding wire, and ER50-6 low carbon steel welding wire in this experiment, as shown in Table 2.

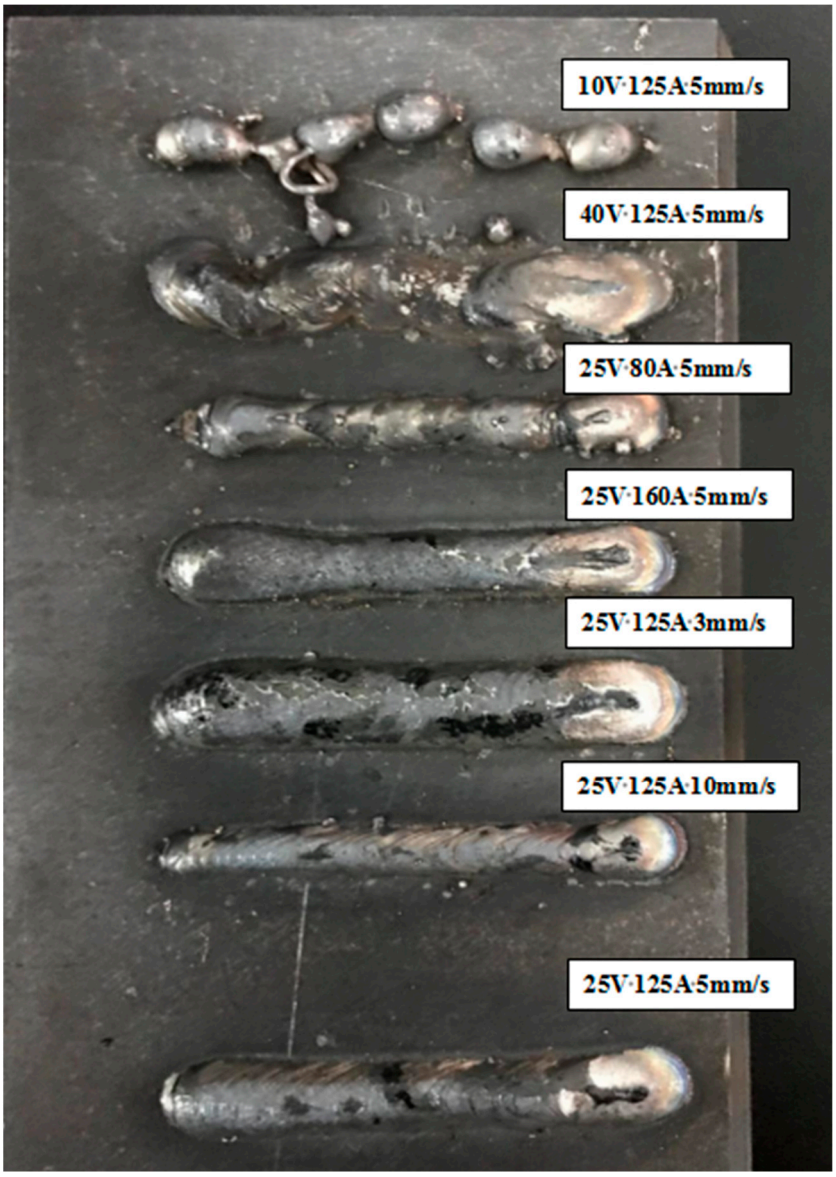

Figure 3. Single-layer single-pass weld shapes with various process parameters.

Table 2. Arc additive manufacturing process parameters.

Process Parameters	Wire Type	
	ER304	ER50-6
Welding voltage	23 V	20 V
Welding current	125 A	110 A
Welding speed	5 mm/s	5 mm/s
Protective gas type and composition	95% Ar + 5% CO_2	100% CO_2
Protective gas flow	18 L/min	16 L/min
Wire diameter	10 mm	10 mm

3. Results and Discussion

3.1. Macroscopic Morphology and Microstructure of Stainless-steel Specimens

Figure 4 shows a deposited sample produced by ER304 stainless-steel wire. It can be seen that the bead surface was smooth, and the overlap fusion between the welds was sound, without collapse.

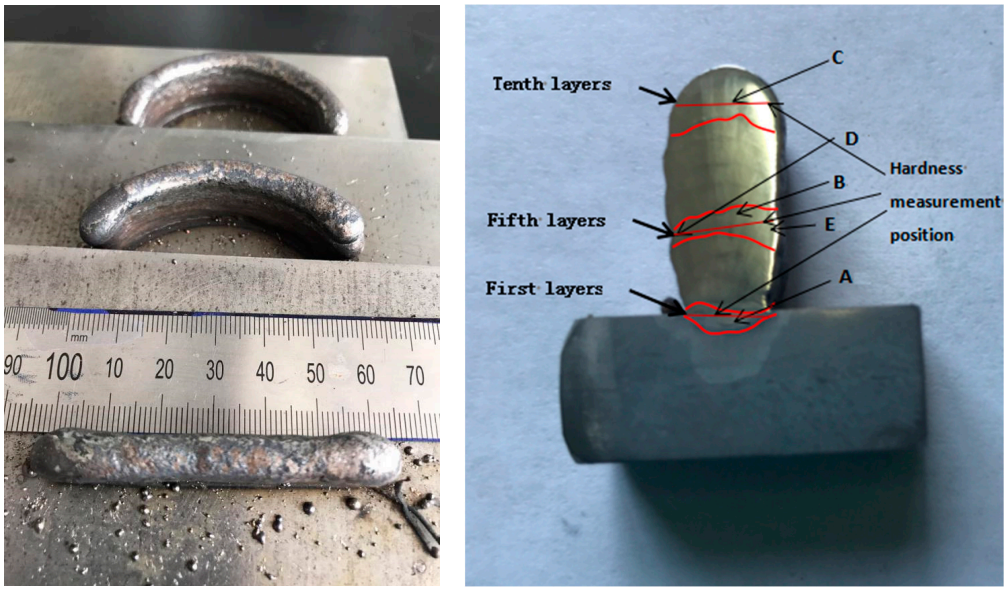

Figure 4. Wire arc additive manufacturing (WAAM) stainless-steel wall. (**a**) The three-types of curvature of the samples; (**b**) examination cross-section (A: middle of the first layer; B: middle of the fifth layer; C: middle of the tenth layer; D: inside area of the fifth layer; E: outside area of the fifth layer).

Figure 5a–c show the metallographic microstructures of the A, B and C regions shown in Figure 4, of the curvature 0 sample, respectively. The white part in the figures is austenite, and the black part is ferrite. Meanwhile, from the crystal morphology, region A was mainly fine cell crystal. Region B was mainly coarse dendrites and had secondary dendrites. Besides, its dendrite spacing was significantly larger than that of region A. Region C is mainly composed of free-form equiaxial crystals.

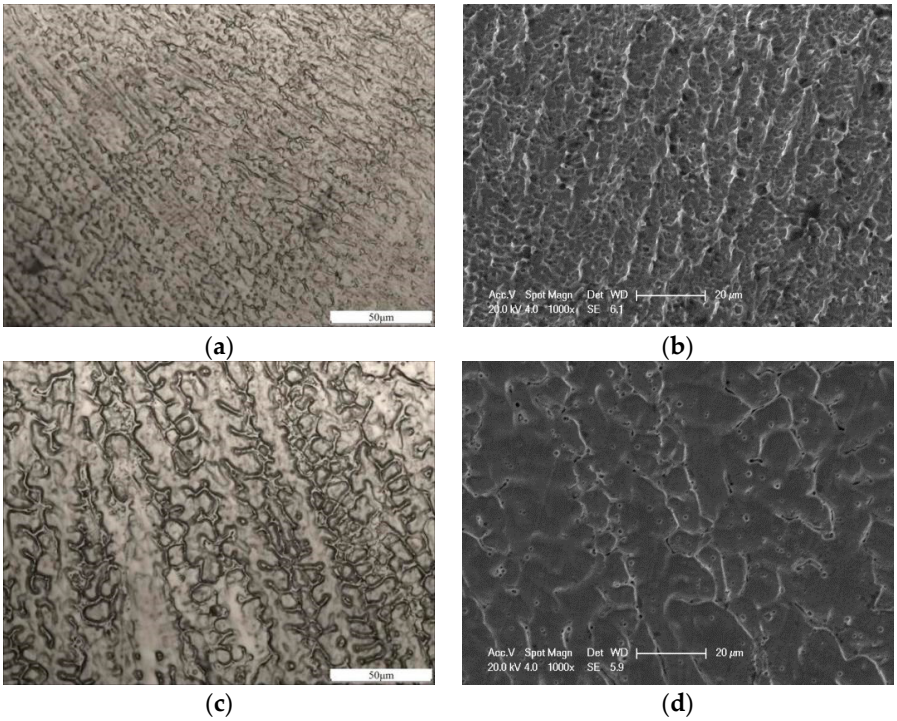

Figure 5. *Cont*.

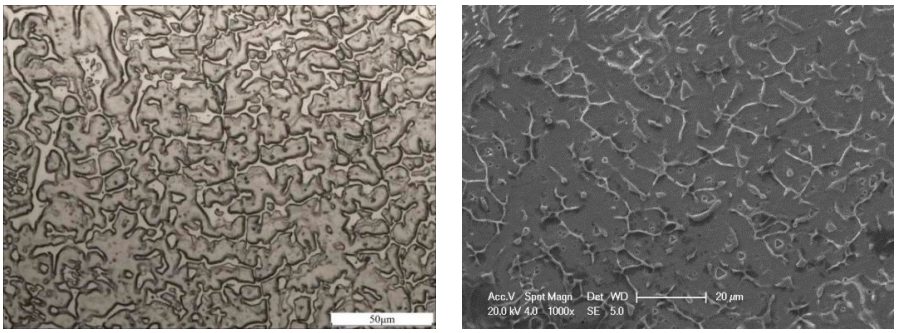

(**e**) (**f**)

Figure 5. Metallographic structures of the curvature 0 sample. (**a**) metallographic microscope optical image at the bottom of the sample; (**b**) SEM micrograph at the bottom of the sample; (**c**) metallographic microscope optical image at the middle of the sample; (**d**) SEM micrograph at the middle of the sample; (**e**) metallographic microscope optical image at the top of the sample; (**f**) SEM micrograph at the top of the sample.

The ratio of the temperature gradient (G) to the growth rate (R) determines the mode of solidification, and the microstructure after solidification [25]. $R = \nu\cos\alpha$, and α is related to the distance to the centreline, here ν denotes the welding speed. In Figure 5, the positions of the bottom, middle and top metallographic structures are located on a vertical line, and the distances from the centre line are basically the same. It can be considered that the growth rates (R) of the three parts are similar, and that the value of G/R is approximately depended on G. Due to the heat dissipation of the substrate, the temperature gradient G at the bottom of the additive parts was maximized, and the G/R was also the largest. Hence, it was a mainly planar structure and composed of cellular crystal at the bottom, as shown in Figure 5a,b. As the height of the deposited layer was increased, the temperature gradient G in the middle was smaller than that in the bottom, and the G/R in the middle was also smaller than that of the bottom, due to the preheating effect of the previously formed layer. The middle was mainly dendrites, as shown in Figure 5c,d. Due to the heat accumulation of the formed portion, both the temperature gradient G and the G/R ratio of the top portion were the smallest. In addition, the heat dissipation direction of the molten pool at the top was changed, so the top portion was mainly equiaxed dendrite, as shown in Figure 5e,f.

Figure 6a,b are the inside and outside metallographic structures of the fifth layer of the curvature 1 sample (position D and E in Figure 4b). Figure 6c,d are the inside and outside metallographic structures of the fifth layer of the curvature 2 sample. It could be seen that the dendrite spacing and the secondary dendrite spacing in the middle inside site were larger than that of the middle outside.

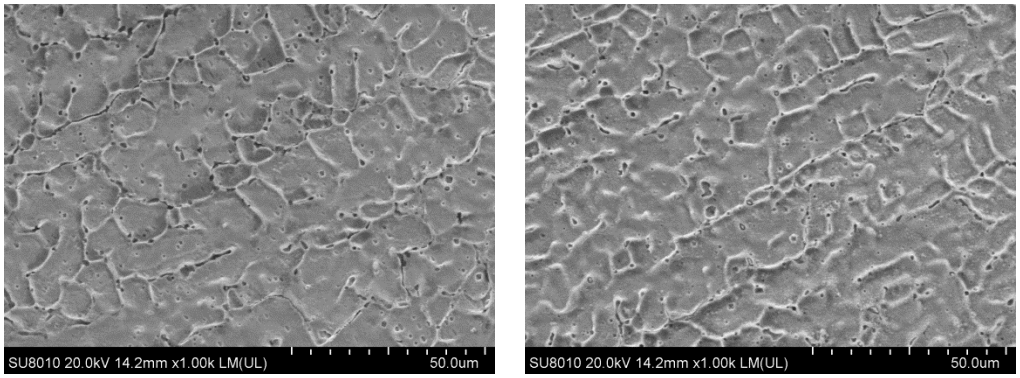

(**a**) (**b**)

Figure 6. *Cont.*

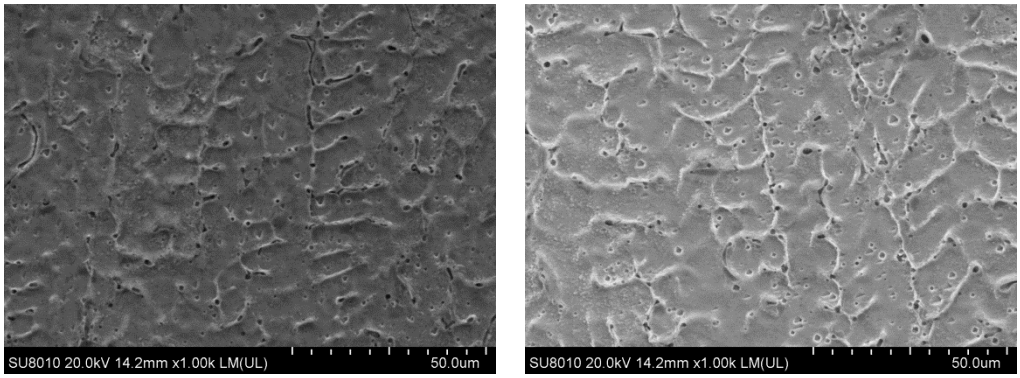

(**c**) (**d**)

Figure 6. Microscope morphology of the two sides in the fifth layer for the curvature 1 and curvature 2 samples. (**a**) the inside for the curvature 1 sample; (**b**) the outside for the curvature 1 sample; (**c**) the inside for the curvature 2 sample; (**d**) the outside for the curvature 2 sample.

For curved passes, the radius at the inside and outside sites is different [26], as shown in Figure 7. According to the test conditions, the width of the single-pass multi-layer additive was about 6mm, and the welding speed of the experiment was 5 mm/s. Thus, from the formula

$$v_o = \frac{v}{R}(R+3), v_i = \frac{v}{R}(R-3) \quad (1)$$

v_o: actual welding speed of outside; v_i: actual welding speed of inside; v: actual welding speed. It was concluded that for v_o, the curvature 1 sample was equal to 5.3 mm/s, and v_i was equal to 4.7 mm /s. v_o of the curvature 2 sample was equal to 5.5 mm/s, and v_i was equal to 4.5 mm/s.

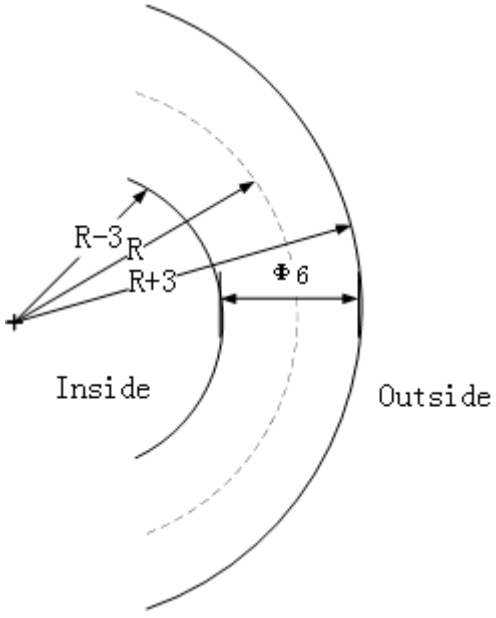

Figure 7. Schematic diagram of the weld path for a specific curvature.

Therefore, the actual welding traveling speed on the outside was higher than that of the inside. Under the same welding parameters, higher welding speeds on the outside made the heat input relatively small, and the cooling rate relatively high, resulting in a small pitch of dendrites on the outside, and a finer grain size. Meanwhile, it can be seen in Figure 6 that the difference in grain size between the inside and the outside of the curvature 2 sample is not apparent, compared to that of the curvature 1 sample. There were two reasons for this phenomenon. Firstly, in the process of forming a

curved path for arc additive manufacturing, a magnetic field would be generated in the adjacent area. The magnetic field density in the inside is larger than that of the outside, which causes the direction of arc thrust to be directed to the outside [27]. The asymmetry of this force causes the asymmetry of the droplet [28], which results in a transport of heat input to the outside [29]. Whereas the effect of heat input, caused by the difference in speed between the inside and outside, was offset by the magnetic arc blow. Secondly, a higher effect of magnetic arc blow could be obtained by the larger curvature.

3.2. Microhardness Distribution of Stainless-steel Samples

Figure 8 shows the microhardness distribution result. The hardness values of the first and fifth layers were mostly distributed above 200 HV, which were higher than that of the 304 stainless-steel substrate. This indicates that the microstructure of the first and fifth layers was denser and more uniform than that of the 304 stainless-steel substrate. Meanwhile, the hardness of the tenth layer was rather less than 200 HV, which was caused by its slightly lower compactness, than that of 304 stainless-steel. From the overall observation and analysis, the hardness of the first layer was greater than that of the fifth and tenth layers. Moreover, the fifth layer was slightly harder than that of the tenth layer. Generally, hardness is related to the grain size, carbide particle size and their distribution. Due to the conventional heat dissipation of the substrate, the bottom layer of weld metal had the fastest cooling rate, the smallest weld grain, and the highest micro-hardness. Figures 9 and 10 show the elemental distribution mapping of the middle layer and top layer with EDS analysis. It can be seen that the concentration of Cr and C in the grain boundary position was slightly higher than that in the inner region of the grain. The trend of the top layer was more obvious than that of the middle layer. This elemental distribution originates from the relatively slow cooling rate of the top layer. It had sufficient time to precipitate more carbides at the grain boundaries, and cause the carbon content in the inner region of the grains to be relatively small, which slightly decreased the micro-hardness value. However, in the middle layer, the cooling rate was slightly faster, causing more carbide particles to remain within the grains, and less precipitation to the grain boundaries. Hence, the hardness of the middle layer was slightly higher than that of the top layer.

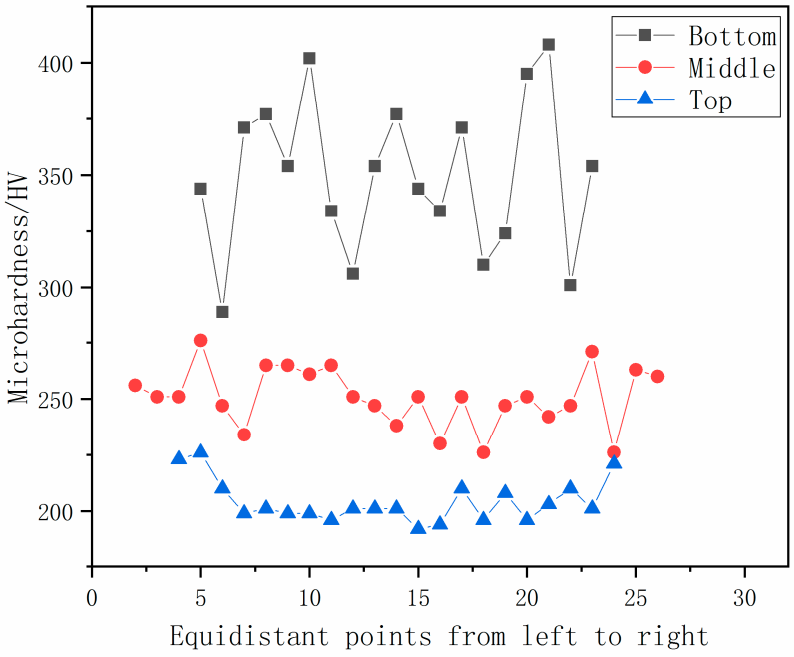

Figure 8. Transverse microhardness distribution of top, middle and bottom of the curvature 0 sample.

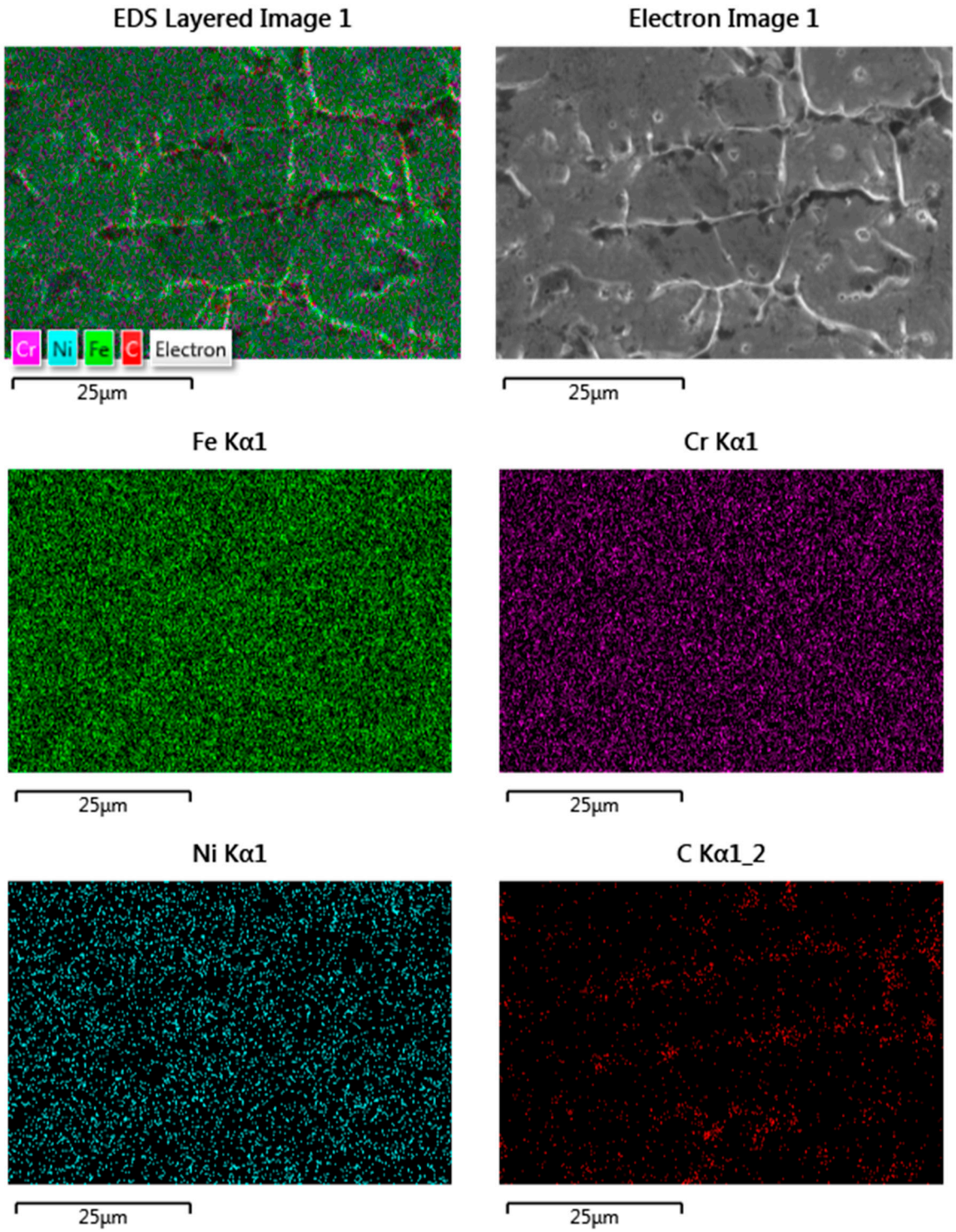

Figure 9. Elemental distribution of the top layer mapped by EDS.

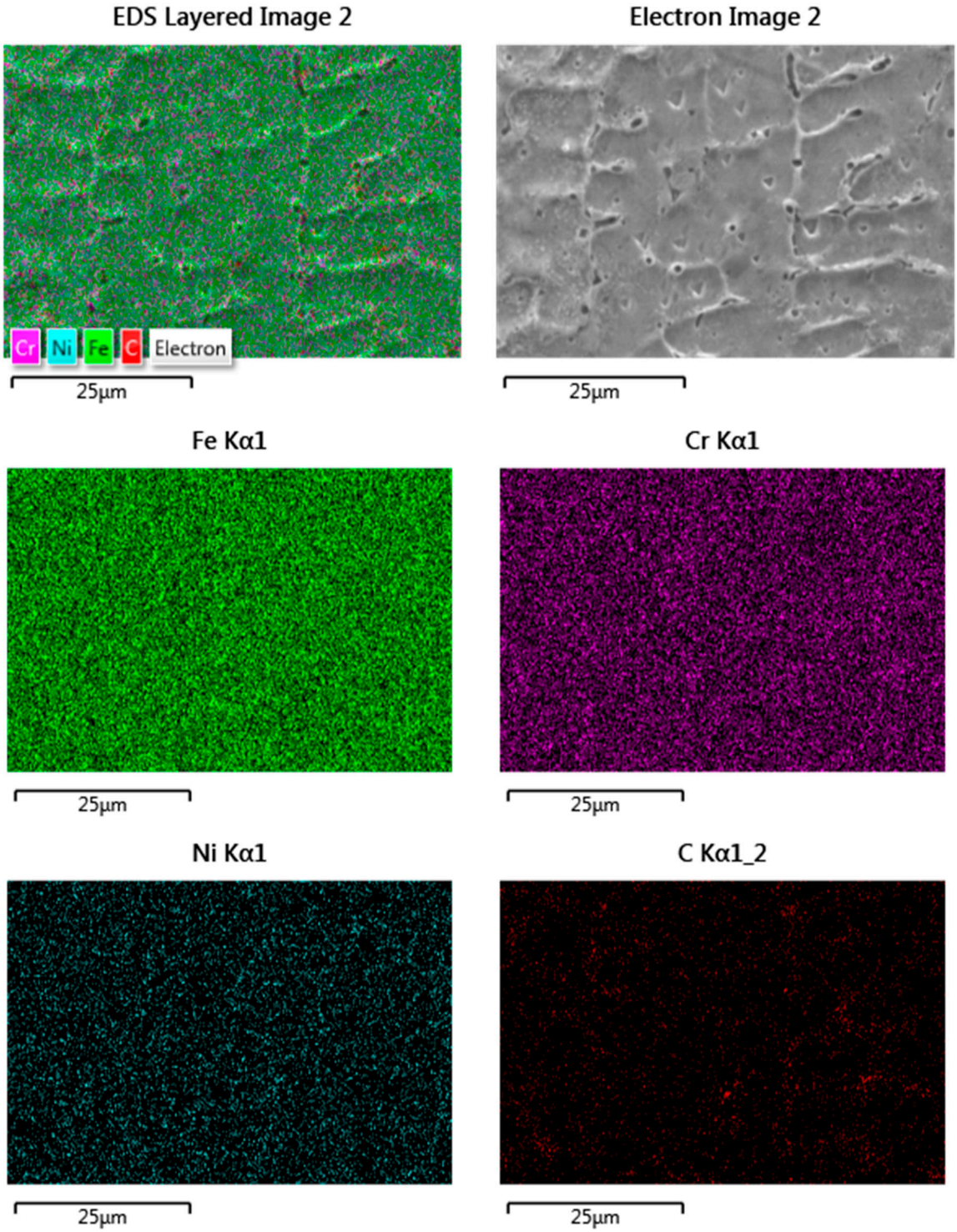

Figure 10. Elemental distribution of the middle layer mapped by EDS.

Figure 11 shows the lateral hardness distribution from inside to outside. The curvature 0 sample was relatively even in terms of hardness distribution, while both the curvature 1 and curvature 2 samples had a rising trend from inside to outside. Besides, it can be seen that the trend of the curvature 2 sample tended to be gentler than that of the curvature 1 sample, as the difference in hardness between the two sides of the curvature 2 sample was smaller than that of the curvature 1 sample. This result also corresponds to the metallographic microstructure shown in Figure 6.

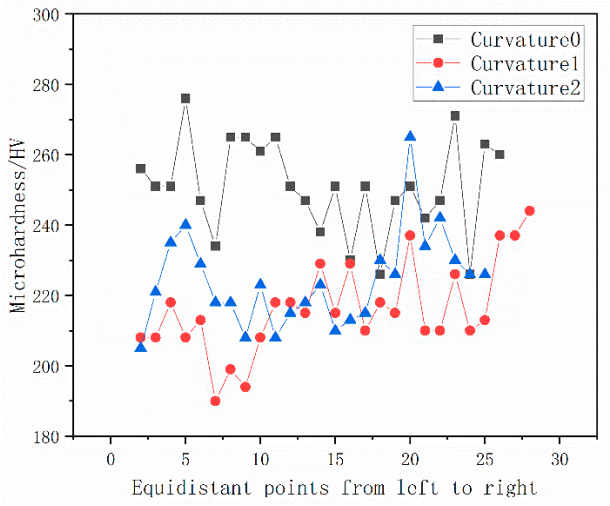

Figure 11. Transverse microhardness distribution in the middle of the curvature 0, 1, and 2 samples.

3.3. Microstructure of the Low Carbon Steel Sample

The metallographic structure of the WAAM low carbon steel sample is shown in Figure 12. When the curvature was small, the difference of grain size between inside and outside was larger. When the curvature increased, the difference of grain size between inside and outside decreased, but the grain size inside was still larger than that found in the outside. The reason that the structure and properties of additive manufacturing parts were affected by curvature, was considered to be the difference in actual welding traveling speed between the inside and outside. With the increasing of curvature, the enhanced effect of the magnetic arc blow reduced the difference in grain size between the inside and outside, owing to a difference in velocity.

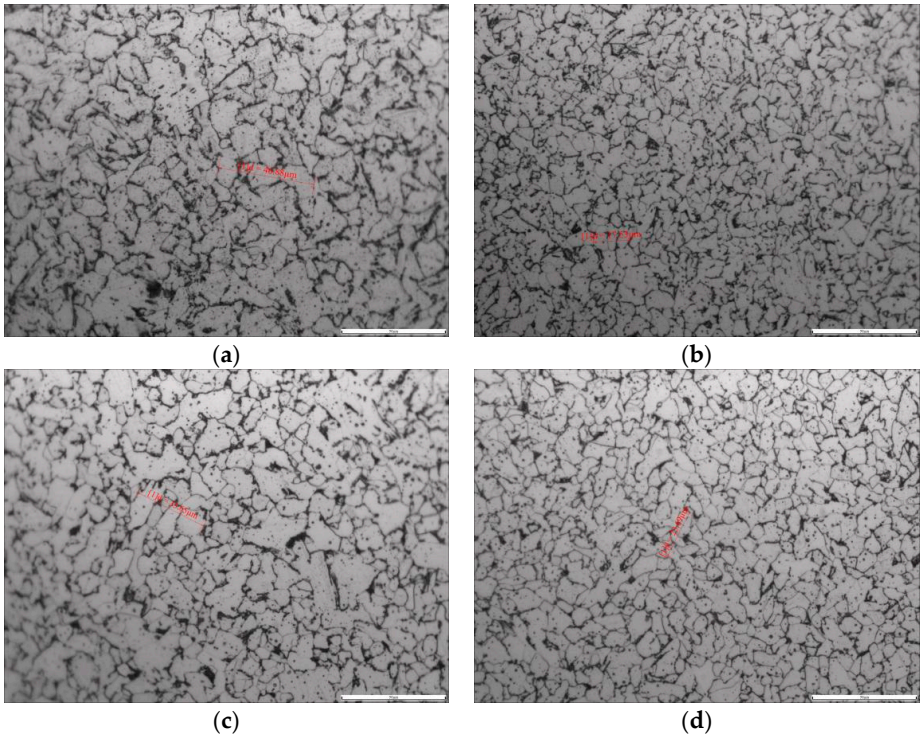

Figure 12. Curvature 1 and curvature 2 samples microstructure on the inside and outside of the fifth layer. (**a**) Curvature 1 sample inside; (**b**) Curvature 1 sample outside; (**c**) Curvature 2 sample inside; (**d**) Curvature 2 sample outside.

4. Conclusions

This investigation prepared stainless-steel and carbon steel thin-walled specimens with different curvatures, by a wire arc additive manufacturing method. Studies shows that trajectory curvature has an apparent influence on the microstructure and performance of thin-walled samples, in different local regions, which can be summarized as:

- The top layer has a slow cooling rate. More carbides particles are precipitated at the grain boundaries, rather than within the grains, and the microhardness value is slightly lower than that of the middle layer.
- Different trajectory curvature leads to a difference in microstructure and properties for inner and outer regions, which originates from the difference in heat input, due to the difference in the actual welding traveling speed between the inside and outside regions.
- As curvature increases, the enhanced effect of the magnetic arc blow reduces the difference in heat input, due to the difference in actual welding traveling speed between the inside and outside areas.

Author Contributions: Investigation, S.Y. and Z.B.; methodology, Z.T. and X.H.; software, Y.C.; writing—original draft, T.F.; writing—review & editing, L.W.

Funding: This research was funded by National Natural Science Foundation of China No. 50901033.

Acknowledgments: This work was supported by the National Natural Science Foundation of China (No. 50901033) and funds from the Hubei Provincial Key Laboratory of Green Materials for Light Industry ((2013)2-6, (2013)2-14).

Conflicts of Interest: The authors declare no conflict of interest.

References

1. Horii, T.; Kirihara, S.; Miyamoto, Y. Freeform fabrication of superalloy objects by 3D Micro welding. *Mater. Des.* **2009**, *30*, 1093–1097. [CrossRef]
2. Frazier, W.E. Metal additive manufacturing: A review. *J. Mater. Eng. Perform.* **2014**, *23*, 1917–1928. [CrossRef]
3. Baufeld, B.; Biest, O.V.D.; Gault, R. Additive manufacturing of Ti-6Al-4V components by shaped metal deposition: Microstructure and mechanical properties. *Mater. Des.* **2010**, *31*, 106–111. [CrossRef]
4. Spencer, J.D.; Dickens, P.M.; Wykes, C.M. Rapid prototyping of metal parts by three- dimensional welding. *Proc. Inst. Mech. Eng. Part B J. Eng. Manuf.* **1998**, *212*, 175–182. [CrossRef]
5. Zhang, H.; Wang, X.; Wang, G.; Zhang, Y. Hybrid direct manufacturing method of metallic parts using deposition and micro continuous rolling. *Rapid Prototyp. J.* **2013**, *19*, 387–394. [CrossRef]
6. Zinoviev, A.; Zinovieva, O.; Ploshikhin, V.; Romanova, V.; Balokhonov, R. Evolution of grain structure during laser additive manufacturing simulation by A cellular automata method. *Mater. Des.* **2016**, *106*, 321–329. [CrossRef]
7. Liu, F.; Xin, L.; Song, M.; Yang, H.; Song, K.; Guo, P.; Huang, W. Effect of tempering temperature on microstructure and mechanical properties of laser solid formed 300M steel. *J. Alloy. Compd.* **2016**, *689*, 225–232. [CrossRef]
8. Kobryn, P.A.; Semiatin, S.L. Microstructure and texture evolution during solidification processing of Ti-6Al-4V. *J. Mater. Process. Technol.* **2003**, *135*, 330–339. [CrossRef]
9. Nowotny, S.; Scharek, S.; Beyer, E.; Richter, K.H. Laser beam build-Up welding: Precision in repair, surface cladding, and direct 3D metal deposition. *J. Therm. Spray Technol.* **2007**, *16*, 344–348. [CrossRef]
10. Katou, M.; Oh, J.; Miyamoto, Y.; Matsuura, K.; Kudoh, M. Freeform fabrication of titanium metal and intermetallic alloys by three-dimensional micro welding. *Mater. Des.* **2007**, *28*, 2093–2098. [CrossRef]
11. Debroy, T.; Wei, H.; Zuback, J.; Mukherjee, T.; Elmer, J.W.; Milewski, J.O.; Beese, A.M.; Wilson-Heid, A.; De, A.; Zhang, W. Additive manufacturing of metallic components—Process, structure and properties. *Prog. Mater. Sci.* **2018**, *92*, 112–224. [CrossRef]
12. Segura, I.A.; Murr, L.E.; Terrazas, C.A.; Bermudez, D.; Mireles, J.; Injeti, V.S.V.; Li, K.; Yu, B.; Misra, R.D.K.; Wicker, R.B. Grain boundary and microstructure engineering of Inconel 690 cladding on stainless-steel 316L using electron powder bed fusion additive manufacturing. *J. Mater. Sci. Technol.* **2019**, *35*, 351–367. [CrossRef]

13. Mines, R. Parent materials and lattice characterisation for metallic microlattice structures. In *Information and Communication Technologies for Ageing Well and e-Health*; Springer: Cham, Switzerland, 2019; pp. 17–29.
14. Gupta, K. *Near Net Shape Manufacturing Processes*; Springer International Publishing: Cham, Switzerland, 2019; pp. 54–74.
15. Xu, J.; Li, A.; Liu, D.; Wang, H. Research on corrosion resistance and wear resistance of laser cladding Cr3Si/g multi-phase coating. *Chin. J. Lasers* **2016**, *43*, 72–78.
16. Mehrpouya, M.; Dehghanghadikolaei, A.; Fotovvati, B.; Vosooghnia, A.; Emamian, S.S.; Gisario, A. The potential of additive manufacturing in the smart factory industrial 4.0: A review. *Appl. Sci.* **2019**, *9*, 3865. [CrossRef]
17. Yan, X.; Gu, P. A review of rapid prototyping technologies and systems. *Comput. Aided Des.* **1996**, *28*, 307–318. [CrossRef]
18. Clark, D.; Bache, M.R.; Whittaker, M.T. Shaped metal deposition of a nickel alloy for aero engine applications. *J. Mater. Process. Technol.* **2008**, *203*, 439–448. [CrossRef]
19. Williams, S.W.; Martina, F.; Addison, A.C.; Ding, J.; Pardal, G.; Colegrove, P. Wire + arc additive manufacturing. *Mater. Sci. Technol.* **2016**, *3*, 641–647. [CrossRef]
20. Zhao, H.; Zhang, G.; Yin, Z.; Wu, L. A 3D dynamic analysis of thermal behavior during single-pass multi-layer weld-based rapid prototyping. *J. Mater. Process. Technol.* **2011**, *211*, 488–495. [CrossRef]
21. Fachinotti, V.D.; Cardona, A.; Baufeld, B.; Van der Biest, O. Finite-element modelling of heat transfer in shaped metal deposition and experimental validation. *Acta Mater.* **2012**, *60*, 6621–6630. [CrossRef]
22. Liu, S.Y.; Feng, Y.H.; Zhan, B.; Luo, Z.J.; Fang, L.L. Effect of stacking speed on microstructure and properties of carbon steel stacking coating fabricated by plasma arc double-filled additive. *Mater. Mech. Eng.* **2018**, *42*, 69–72. [CrossRef]
23. Zhou, X.M.; Tian, Q.H.; Du, Y.X.; Bai, X.W. Effect of longitudinal steady state magnetic field on surface quality and performance of arc additive forming parts. *J. Mech. Eng.* **2018**, *54*, 84–92. [CrossRef]
24. Ge, J.; Lin, J.; Lei, Y.; Fu, H. Location-related thermal history, microstructure, and mechanical properties of arc additively manufactured 2Cr13 steel using cold metal transfer welding. *Mater. Sci. Eng. A* **2017**, *72*, 144–153. [CrossRef]
25. Kou, S. *Welding Metallurgy*, 2nd ed.; Wiley: Hoboken, NJ, USA, 2003; pp. 163–166.
26. Li, W.; Yang, Q.; Zhang, Z.; Gao, D. Effect of weld curvature radius and tool rotation direction on joint microstructure in friction stir welding casting alloys. *Mater. Des.* **2014**, *53*, 124–128. [CrossRef]
27. Wang, H.F.; Lai, W.X.; Zhang, H.O.; Wang, G.L. Effect of curvature curvature on the morphology of the accumulated layer. *New Technol. New Process* **2018**, *8*, 46–49.
28. Zhou, X.M.; Zhang, H.O.; Wang, G.L.; Bai, X.W. Simulation of the influences of surface topography of deposited layer on arc shape and state in arc based additive forming. *Acta Phys. Sin.* **2016**, *65*, 331–342.
29. Zhou, X.; Zhang, H.; Wang, G.; Bai, X. Three-dimensional numerical simulation of arc and metal transport in arc welding based additive manufacturing. *Int. J. Heat Mass Transf.* **2016**, *103*, 521–537. [CrossRef]